Available online at www.sciencedirect.com

jmr&t Journal of Materials Research and Technology

www.jmrt.com.br

Original Article

Simulation of unconstrained solidification of A356 aluminum alloy on distribution of micro/macro shrinkage

Hossein Bayani, Seyed Mohammad Hossein Mirbagheri, Mojtaba Barzegari, Sadegh Firoozi*

Department of Mining and Metallurgical Engineering, Amirkabir University of Technology, Tehran, Iran

ARTICLE INFO

Article history:
Received 20 May 2013
Accepted 17 October 2013
Available online 11 February 2014

Keywords:
Computational Fluid Dynamics
Creeping flow
Reynolds number
Micro-permeability
Unconstrained solidification
Nucleation
Growth

ABSTRACT

In the condition of Newtonian heat transfer, A356 aluminum alloy is solidified with randomly distributed equiaxed dendrites. Ability of interdendritic liquid flow is described by permeability parameter using Darcy's law and this parameter is used to predict the micro-shrinkages. In this study the interdendritic liquid flow during nucleation and grain growth are simulated in a 1 mm × 1 mm domain. Temperature gradient is zero in the initial condition of the unconstrained solidification. The numerical simulation procedure includes two stages; first, numerical evolution of the shape, number, size, and distribution of dendrites during solidification using a novel Cellular Automation Finite Volume (CA-FV) method, and second, numerical determination of the micro-permeability by a Computational Fluid Dynamics (CFD) technique. Subsequently, the effect of Reynolds number, cooling rate and solidification rate on a critical permeability range was investigated in order to predict the micro/macro shrinkage distribution. Results showed that it is possible to propose a mathematical model to relate the Reynolds number and liquid flow rate, in the creeping flow range, on the micro-permeability during unconstrained solidification.

1. Introduction

Nucleation and grain growth occur successively during solidification of alloys and consequently the number, size, distribution and morphology of the grains are determined during this process. In the case of rapid solidification the effect is more pronounced. During solidification, micro-defects such as micro-segregation, micro-porosities and micro-shrinkage form a porous medium (mushy zone) located in interdendritic spaces. The ability of the liquid to flow into the mushy zone is known as permeability of interdendritic liquid. Therefore, micro-defects formation is affected by the permeability factor. In a number of studies, micro/macro solidification models have been simulated based on the permeability factor using Darcy's law [1–4].

To obtain an expression for the permeability as a function of the porosity of the porous medium, one generally considers flow through an idealized medium geometry, since it is impractical to solve the flow equations for the complex flow between the particles [5–7]. Analysis of permeability for Stokes flow through periodic arrays of cylinders was done by Sangani and Acrivos [8], Sparrow and Loefler [9], and Larson and Higdon [10].

* *Corresponding author.*
E-mail: smhmirbagheri@aut.ac.ir (S.M.H. Mirbagheri).

2238-7854 http://dx.doi.org/10.1016/j.jmrt.2013.10.011

The pressure drop required to drive the flow is a function of Reynolds number. Several authors computed the fluid flow through periodic arrays of cylinders as the function of Reynolds numbers for three ranges of low, moderate, and high Reynolds number [11–20]. Particularly important is the work of Koch and Ladd [11] for modeling micro-permeability and drag force based on Reynolds number using a Lattice-Boltzmann formulation. Also McCartney [19] calculated the micro-permeability in the range of low Reynolds numbers up to about 150 by Lattice Gas Cellular Automata (LGCA) model.

These models have an important application in the mathematical modeling of flow through arrays of dendrites during solidification of mushy alloys. There are many investigations for experimental measuring of permeability during solidification process [21–27]. However, the experimental goal is to measure the permeability and the temperature of an alloy during solidification and to correlate the permeability with the solid fraction [27].

Piwonka and Flemings [28], Apelian et al. [24], Streat and Weinberg [21], Liu et al. [29] and Murakami et al. [23] reported the permeability in equiaxed dendritic structures. Ganesan and Poirier [4] and Poirier and Ocansey [25] measured and reported the permeability as an inverse function of the specific area of the solid selected as the length scale in equiaxed microstructures based on Kozeny–Carman model. Brown et al. [30] developed a numerical model for the simulation of 3D flow through equiaxed dendrites of an $Al_{13}Cu_3Si$ alloy and determined the variation in permeability of structure as solidification progressed. They modeled the evolution of an equiaxed dendrite and calculated the permeability from Darcy's law using a CFD program. Madison et al. developed a 3-D permeability simulation for a fine domain in a constrained solidification and evaluated the simulation results with experimental results [31].

In spite of these valuable contributions in this field, determination of dendritic structural permeability and micro-shrinkage due to the complex microstructure of the dendrites still remains a challenge in both fields of mathematical and experimental methods. It appears that critical ranges for permeability exist in which the micro-shrinkages form.

In this paper, a numerical model has been introduced for determination of liquid flow micro-permeability through dendritic solid network during grain growth for either a small section of a droplet or a cell from solidification front, in the Newtonian heat transfer condition. The model includes five stages; first, numerical simulation of nucleation and growth of the equiaxed grains using a CA-FV method, second, numerical simulation of micro fluid flow for interdendritic liquid alloys using CFD code, third, calculation of micro-permeability based on modified Darcy's law using the pressure and velocity results of the CFD code, forth, neural network training for permeability prediction in various condition and fifth, micro porosity prediction in 2D domain. These results can be used as a module in a commercial casting code in order to predict the micro-defects such as micro porosities, shrinkages or micro-segregations. In fact, in solidification numerical simulation codes, the present model could be used for all meshes adjacent to the solid/liquid interface as a fine porous boundary layer based on a critical range series of the micro-permeability.

2. Computation models and assumptions

In the present work, two separate computation models of the nucleation/grain growth and the interdendritic liquid flow have been developed and coupled for predicting the micro-permeability and characterization of effective parameters for a symmetric domain as a 2D section. This is achieved by combining sub-models for each of these processes. One is a computation CA-FV. The other is a micro fluid flow by using the CFD model for calculation of the interdendritic micro-permeability. The governing equations are described in detail in the next sections. Significant assumptions are:

(1) For a fine domain during solidification a boundary layer is introduced at liquid/solid interface.
(2) Temperature gradient in the boundary layer is equal to zero.
(3) Heat transfer in the liquid interface is Newtonian.
(4) Prior to the nucleation the under-cooling throughout the boundary layer is constant, and after nucleation it is negative due to the liberation of latent heat of solidification at solid/liquid interface.
(5) Nucleation in the boundary layers is fully equiaxed.
(6) The heat transfer and solidification in transverse direction of the boundary layer is assumed two dimensional, since the boundary layer around each grain is very thin.

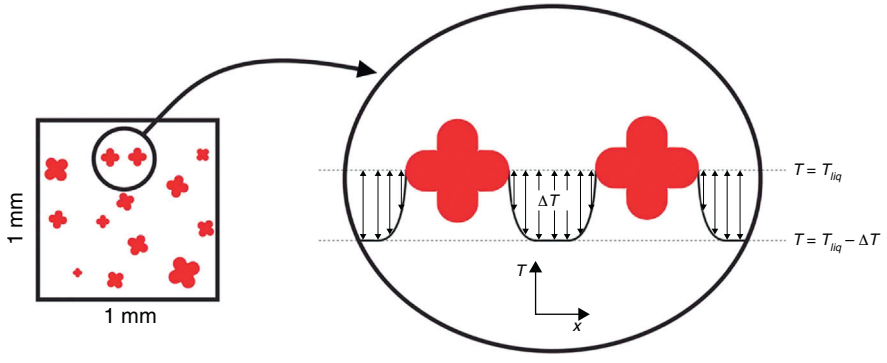

Fig. 1 – Newtonian condition, temperature distribution around the equiaxed nuclei.

2.1. Nucleation and grain growth code

2.1.1. Governing equations and solving procedure

Nucleation and grain growth code that has been developed in this paper is based on the CA model [32,33], which is an unconstrained nucleation and grain growth model. The model comprises of: (1) Stochastic nucleation rate based on local under-cooling, and (2) nuclei growth based on slope of the local temperature [34,35]. However, in the present work, for a binary alloy system in the mushy zone, it is assumed that there is no constitutional under-cooling during grain growth. Number, distribution, morphology of nuclei, and growth rate are controlled by thermal under-cooling and its derivative, which is formed by Newtonian's heat transfer in a micro two dimensional (2D) space. In this condition, at the beginning, all liquid have the same under-cooling, i.e., the gradient of the under-cooling or the liquid temperature slope is equal to zero before nucleation. As shown in Fig. 1 once the nucleation takes place, temperature around the nuclei is raised, because of the liberation of the latent heat. Therefore, the local temperature gradient around the grains is negative after the nucleation.

After the solidification, the microstructure of the solidified alloy will consist of fully equiaxed grains and no columnar grains. Therefore, in this investigation for the A356 mushy alloy, initial and boundary conditions for simulation of heat transfer and liquid flow for a 1 mm × 1 mm domain are based on the unconstrained solidification and the Newtonian's heat transfer, with no micro segregation.

(i) Heat transfer equations

The heat transfer equation for this mushy zone may be written as:

$$\rho C_p \frac{\partial T}{\partial t} = k\nabla^2 T + \rho \Delta H_f \frac{\partial f_s}{\partial t} \tag{1}$$

$$f_s = 1 - \left[\frac{T - T_{sol}}{T_{liq} - T_{sol}}\right]^{-1/(1-k_0)} \tag{2}$$

where ρ, C_p and k are the density, heat capacity and thermal conductivity, respectively; f_s is solid fraction, k_0 is the partition coefficient and T_{sol}, T_{liq} are solidus and liquidus temperature, respectively. $\rho\Delta H_f(\partial f_s/\partial t)$ is the latent heat term, which is a function of temperature between the solidus and the liquidus, and is written as follows:

$$\rho \Delta H_f \frac{\partial f_s}{\partial t} = \rho \Delta H_f \frac{\partial f_s}{\partial T}\frac{\partial T}{\partial t} = \rho \Delta H_f \left[\frac{-1}{(T_{liq} - T_{sol})(k_0 - 1)}\right] \times \left[\frac{T - T_{sol}}{T_{liq} - T_{sol}}\right]^{(2-k_0)/(k_0-1')} \left(\frac{\partial T}{\partial t}\right) \tag{3}$$

The fraction of solid in the mushy zone is estimated by Eq. (2). The release of latent heat in the mushy zone is calculated by substituting Eq. (3) into the third term of Eq. (1). Therefore heat transfer equation is given by:

$$\rho(C_P^{eq})\frac{\partial T}{\partial t} = \nabla \cdot (k\nabla T) \tag{4}$$

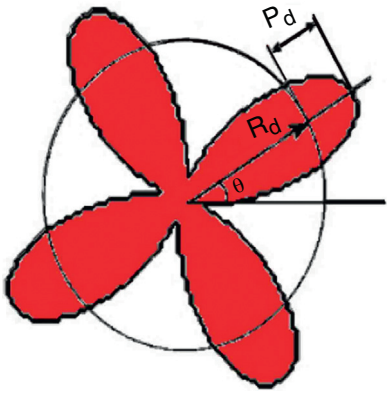

Fig. 2 – Shape and 4 crystalline directions of a nucleus at the beginning of the growth.

where C_P^{eq} can be considered a quasi-specific heat capacity given by:

$$C_P^{eq} = \left[C_P - \Delta H_f \left[\frac{-1}{(T_{liq} - T_{sol})(k_0 - 1)}\right]\left[\frac{T - T_{sol}}{T_{liq} - T_{sol}}\right]^{(2-k_0)/(k_0-1')}\right] \tag{5}$$

Physical properties of the liquid and solid are assumed to be constant above T_{liq} and below T_{sol}, respectively. However, in

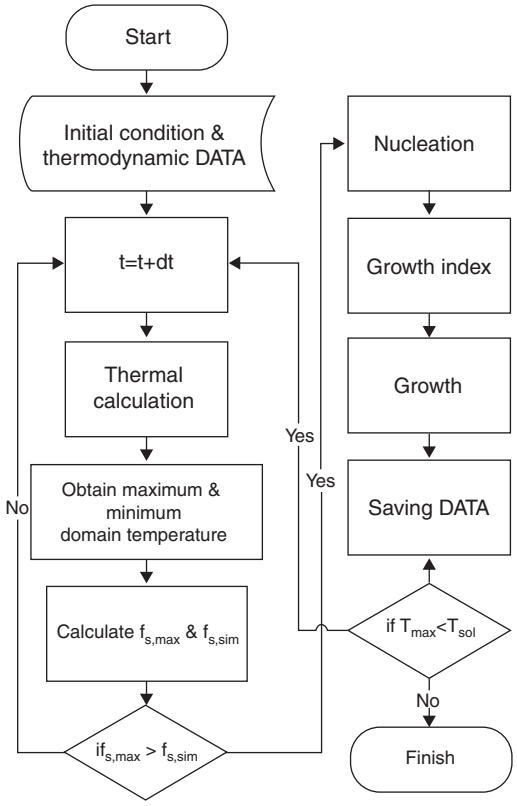

Fig. 3 – Algorithms of Nucleation, grain growth and heat transfer during solidification for the present work.

the mushy zone, coefficients of heat conductivity and thermal capacity are presented as $k_{mu} = f_L k_L + f_S k_S$, and $C_p^{mu} = f_L C_P^l + f_S C_P^S$ [36].

(ii) Nucleation equations

When the temperature falls below the liquidus temperature, nucleation begins. In this condition, the fraction of nuclei (I_s) at each temperature and time are calculated from Eq. (6), as follows:

$$I_s = A\ \exp\left(\frac{BT_{liq}^2}{R\Delta H_f^2 T(T_{liq}-T)^2}\right);\quad T < T_{liq} \tag{6}$$

where A and B are constants and R is the ideal gas constant. After determining the fraction and then number of nuclei in each time step, by assigning a random distribution function, nuclei are distributed in the liquid domain. In the next step, the latent heat of solidification is calculated to adjust the temperature. It is important to note that the latent heat of solidification is released only when the temporary radius of the nucleus becomes greater than a critical radius, r^*, as in Eq. (7).

$$r_t \geq 2\gamma\left(\frac{T_{liq}^2}{\Delta H_f^2(T_{liq}-T)^2}\right) = r^*;\quad T \leq T_{liq} \tag{7}$$

(iii) Grain growth equations

As mentioned before, once stable nuclei are created, a negative temperature gradient forms in liquid adjacent to the grains and equiaxed grains grow as shown in Fig. 1. The direction of primary arms of the equiaxed dendrites depend on crystal structure [37]. Here, a B.C.C. crystal structure is assumed, in which each equiaxed dendrite has four perpendicular primary arms in 2D space, where they can grow in 48 crystalline directions. In order to simulate the morphology of the grain growth, a simple shape was used for grains based on Eq. (8) in polar coordinates. It should be noted, that for the equiaxed grains in polar coordinates, the flow pattern in 3D and 2D space are generally similar.

$$r = R_d + P_d\ \cos(4(\theta+\theta_0))\quad \text{if}\quad 0 < \frac{P_d}{R_d} < 1;\quad (R^*) < hR^* = R_d + P_d \tag{8}$$

Fig. 2 shows a "cloverleaf" morphology for a dendrite section created based on Eq. (8), where P_d is perturbation, R_d radius of spherical nuclei prior to perturbation, and θ angle between primary arm direction and stream line. It is noticeable, in Fig. 2, that solid fraction of the spherical nuclei is equal the cloverleaf nuclei. A function (Eq. (9)) needs to be defined for the dendrites radius growth rate (dr), which is added to the surface of existing grains in each time step of solidification stage.

$$r_{new} = r_{old} + dr;\quad dr = \frac{df_s}{2\pi\sum r} \tag{9}$$

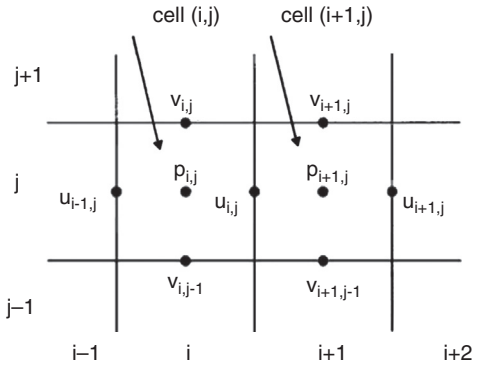

Fig. 4 – Schematic of a staggered mesh and location of vector and scalar variables.

For a solidifying cell, as the solid fraction within the cell becomes greater than zero, the local temperature of the particles is obtained using the relevant phase diagram and the under-cooling is calculated accordingly. In each solidifying cell, the change in solid fraction is primarily determined by KGT model, which calculates the maximum growth rate based on a given under-cooling at near absolute stability limit [35]. A captured liquid cell by a growing neighboring cell is assigned the same grain orientation as its growing neighbor [38]. Fig. 3 shows the CA-FD solution algorithm of heat transfer during nucleation and grain growth. Finally, results of nucleation and grain growth simulation at each df_s, is used in the CFD code to simulate pressure and velocity fields and then calculate the temporary micro-permeability in the 1 mm × 1 mm domain.

2.2. CFD code

2.2.1. Governing equations and solving procedure

(i) Fluid flow equations

The Navier–Stokes and continuity equations in 2D space are used to simulate flow of the interdendritic liquid through

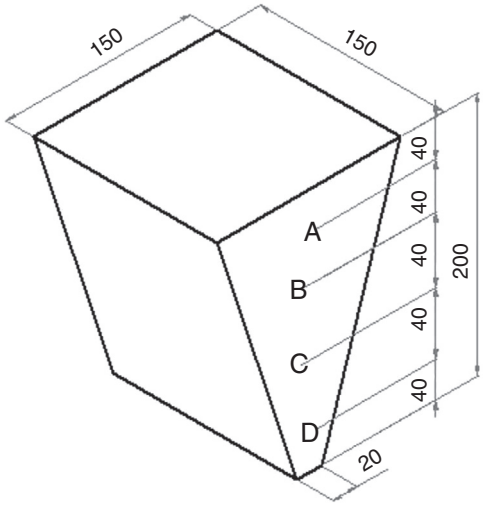

Fig. 5 – Aluminum model for experimental validation and location of metallurgical samples.

the network of equiaxed grains. By introducing the following dimensionless variables the Navier–Stokes and continuity equations are presented in a non-dimensional form [39]:

$$\vec{x}^* = \frac{\vec{x}}{L}, \quad t^* = \frac{u_\infty t}{L}, \quad \vec{u}^* = \frac{\vec{u}}{u_\infty}, \quad \vec{g}^* = \frac{L}{u_\infty^2}\vec{g},$$

$$p^* = \frac{p - p_\infty}{\rho_\infty u_\infty^2} \quad \text{and} \quad Re = \frac{\rho_\infty u_\infty L}{\mu}$$

$$\frac{\partial u}{\partial t} + \frac{\partial p}{\partial x} = \frac{1}{Re}\left(\frac{\partial^2 u}{\partial x^2} + \frac{\partial^2 u}{\partial y^2}\right) - \frac{\partial(u^2)}{\partial x} - \frac{\partial(uv)}{\partial y} + g_x \tag{10a}$$

$$\frac{\partial v}{\partial t} + \frac{\partial p}{\partial x} = \frac{1}{Re}\left(\frac{\partial^2 v}{\partial x^2} + \frac{\partial^2 v}{\partial y^2}\right) - \frac{\partial(uv)}{\partial x} - \frac{\partial(v^2)}{\partial y} + g_x \tag{10b}$$

$$\frac{\partial u}{\partial x} + \frac{\partial v}{\partial y} = 0 \tag{11}$$

The continuity equation is solved implicitly by using the Poisson's equation (Eq. (12)).

$$\nabla^2 P = \frac{1}{\Delta t}\nabla \cdot V^* \tag{12}$$

After solving the Navier–Stokes equations, the calculated pressure and velocity fields were used to obtain the micro-permeability of the 1 mm × 1 mm mushy zone in each growth sequence.

(ii) Permeability equations

Darcy's law is a simple and empirical proportional relationship between the instantaneous discharge rate through a porous medium (V), the viscosity of the fluid (μ) and the pressure drop over a given distance [40].

$$V = -\frac{K}{\mu}\nabla P \tag{13}$$

where K is permeability. Eq. (13) is not valid at high Reynolds number and in this study, an effective Darcy's law equation was used to calculate the micro-permeability (Eq. (14)).

$$V = -\frac{K}{\mu f_l}\nabla P \tag{14}$$

Finally, the governing equations are solved by FVM. The numerical solution method can be considered in four steps: (1) Meshing of the system, (2) Converting the differential equations to finite difference approximation, (3) Solution of the finite volume approximations of momentum in order to calculate the velocity profile and pressure gradient, and

Table 1 – Thermo-physical properties, boundary and initial conditions.

Composition (wt%)	Si = 6
Domain dimensions (mm^2)	1 × 1
Thermal conductivity ($J\,s^{-1}\,m^{-1}\,K^{-1}$)	$K_l = 91$, $K_s = 121$
Heat of fusion ($J\,kg^{-1}$)	$\Delta H_f = 389{,}187$
Kinematic viscosity ($m^2\,s^{-1}$)	$\upsilon = 2.3 \times 10^{-6}$
Specific heat ($J\,kg^{-1}\,K^{-1}$)	$C_p^l = 963$, $C_p^S = 1084$
Density ($kg\,m^{-3}$)	$\rho_L = 2385$, $\rho_S = 2695$
Transformation temperature (°C)	$T_L = 577 \pm 3$, $T_S = 640 \pm 3$
Number of cells	N = 4,000,000
Dimension of each cell (μm)	$\Delta X = \Delta Y = 5$
CPU time (Core2 Dou E8400) (h)	0.5
Boundary condition at locations	(1): Inlet
	(4): Outlet
	(2) and (3): Free-slip boundaries
	(5): No-slip boundaries for internal dendrites' surfaces
	No pressure gradient condition for all boundaries
	$U_{Inlet} = 0.16$ mm/s, $V_{Inlet} = 0$.
	Reynolds number (inlet) = 0.3

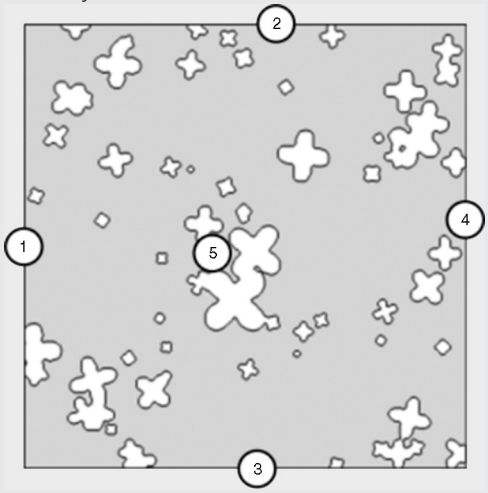

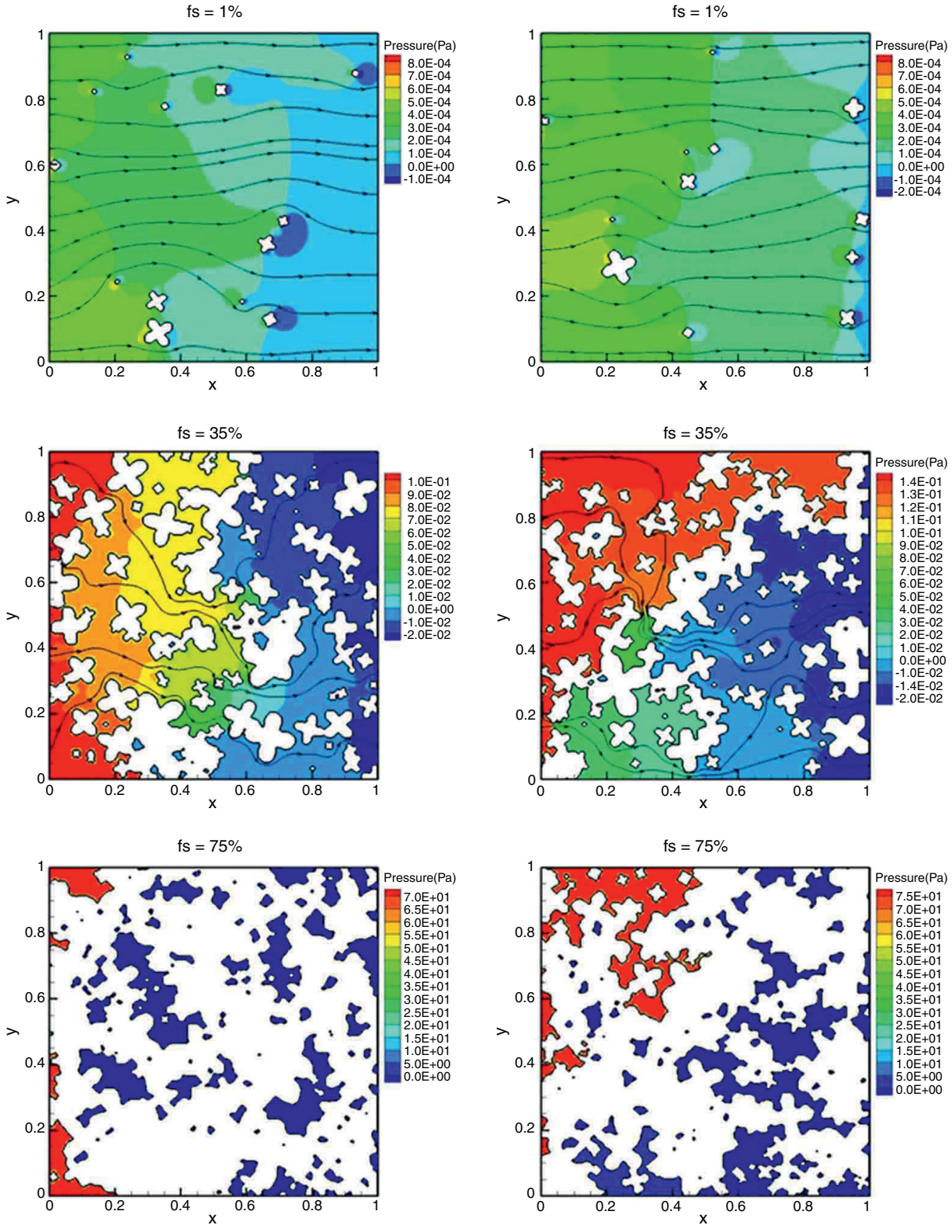

Fig. 6 – Simulation of the pressure fields adjacent to two different nucleus distribution with 1, 35, 75% solid fraction for A356 aluminum alloy, $dQ = 100$ J/s in each time step, $Re = 0.1$, Left: random distribution 1, Right: random distribution 2, dimensions: $x = y = 1$ mm.

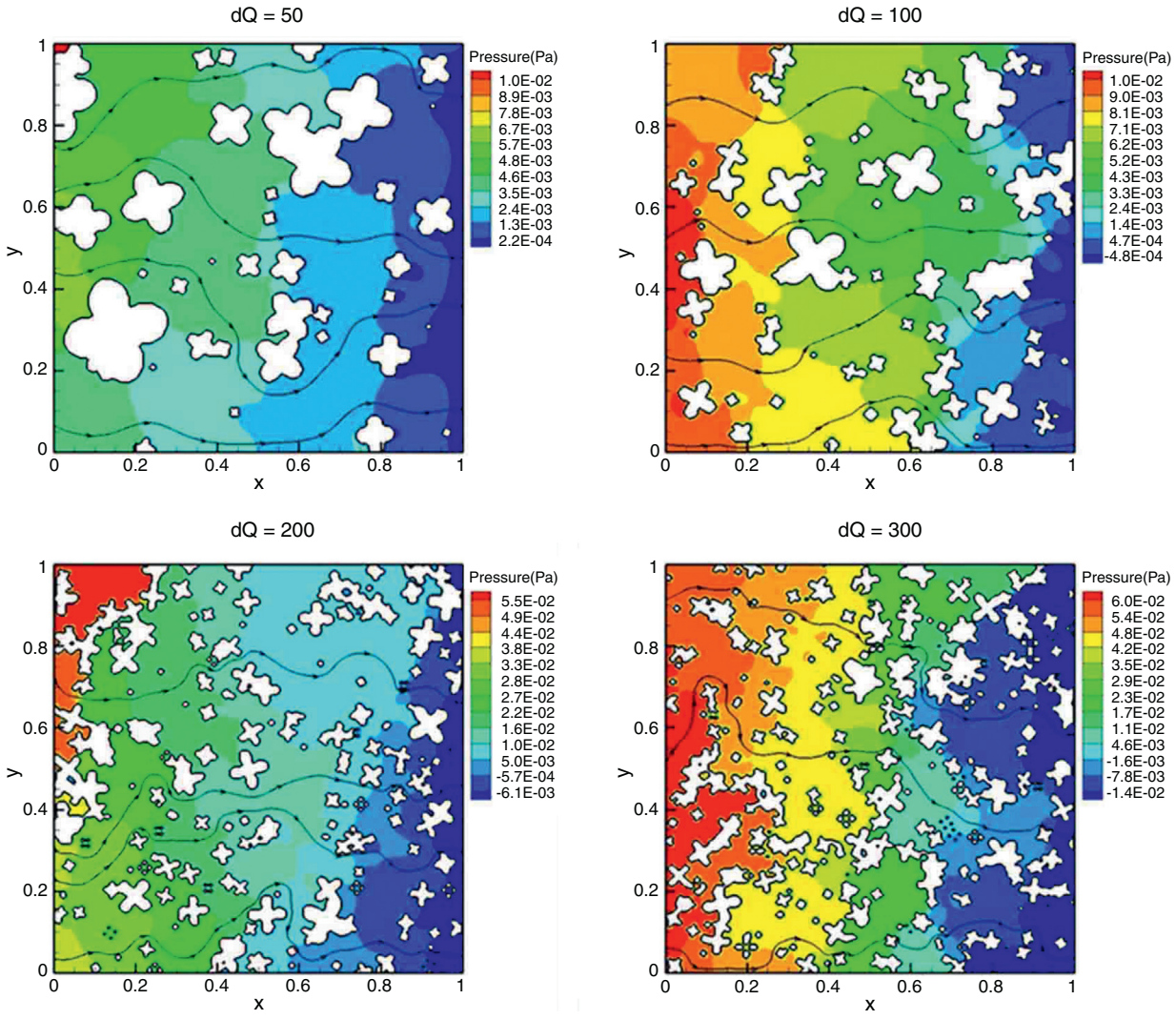

Fig. 7 – Simulation of the pressure field adjacent to 4 types of nucleus distribution for A356 aluminum alloy at low solid fraction ($f_s = 0.2$) and dQ equals to 50, 100, 200, 300 J/s in each time step, $Re = 0.1$, dimensions: $x = y = 1$ mm.

(4) Calculation of micro-permeability of the mushy zone by adding Darcy's law in each growth sequences.

(1) The computational domain is divided into a number of cells with ΔX, ΔY dimensions, and cell dimensions are equal for all calculations. As shown in Fig. 4, domain is discretized as a staggered grid. The continuity equation and the diffusive terms of the momentum equation are discretized using central differencing. The donor-cell scheme was used to discretized the convective terms of momentum equation [41]
(2) Finite volume approximation of momentum equations was constructed according to Griebel et al. [42].
(3) To solve the governing equations of fluid flow, the projection method was used. The projection method uses an auxiliary velocity (V^*) to obtain a Poisson's equation for pressure [42]. This equation was solved using Successive Over-Relaxation (SOR) methods. The momentum equation is split into two independent equations with Eq. (15) with no pressure term and Eq. (16) with pressure term:

$$\frac{V^* - V^n}{\Delta t} + V^n \cdot \nabla V^n = \frac{1}{Re}\nabla^2 V^n \tag{15}$$

$$\frac{V^{n+1} - V^*}{\Delta t} + \nabla P^{n+1} = 0 \tag{16}$$

The continuity equation in time derivative form is:

$$\nabla V^{n+1} = 0 \tag{17}$$

The divergence of Eq. (17) takes the form:

$$\frac{\nabla \cdot V^{n+1} - \nabla \cdot V^*}{\Delta t} + \nabla^2 P^{n+1} = 0 \tag{18}$$

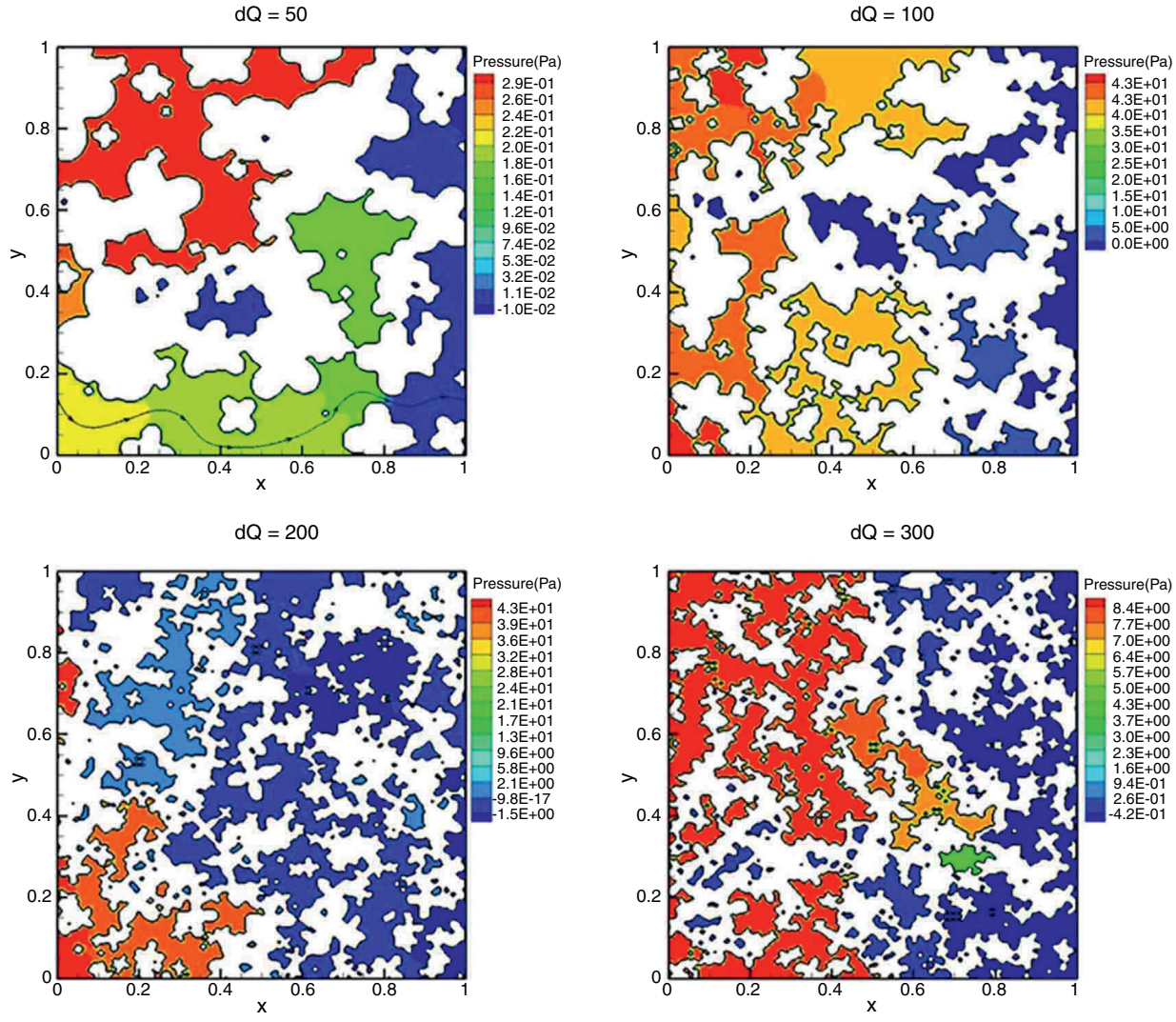

Fig. 8 – Simulation of the pressure field adjacent to 4 types of nucleus distribution for A356 aluminum alloy at high solid fraction ($f_s = 0.55$) and dQ equals to 50, 100, 200, 300 J/s in each time step, $Re = 0.1$, dimensions: $x = y = 1$ mm.

Continuity equation, Eq. (16), requires that ∇V^{n+1} to be zero, thus:

$$\nabla^2 P^{n+1} = \frac{1}{\Delta t} \nabla \cdot V^* \tag{19}$$

The superscripts (n) and ($n+1$) denote old and new time level, respectively. In projection method V^{n+1} domain is calculated at each new time step.

(4) After obtaining the pressure and velocity fields, which is called here as the temporary micro-permeability subroutine, and using Darcy's law, the coefficient of temporary micro-permeability is calculated in each solid fraction. Fig. 3 describes the CFD algorithm used in the present work. The detailed procedure is presented previously in Ref. [43].

All simulations were run using the data in Table 1 for an A356 aluminum alloy for a 1 mm × 1 mm domain.

3. Experimental method

A simple part was considered for simulation and casting (Fig. 5). A numerical model for this part was created and used to simulate with Pro Cast commercial simulation software. The code developed in this research was applied on the numerical model. Another part was casted in metal mold. Metallographic samples were prepared from specified position.

3.1. *Simulation with developed code*

For developed code first the neural network must be trained. So, approximately 250 different conditions were simulated in micro scale. Random nucleation was performed and permeability of domain was calculated by CFD simulation and Darcy law. Calculated data was used for training the neutral network. The trained neutral network module was added in solidification code and predicts probable defects.

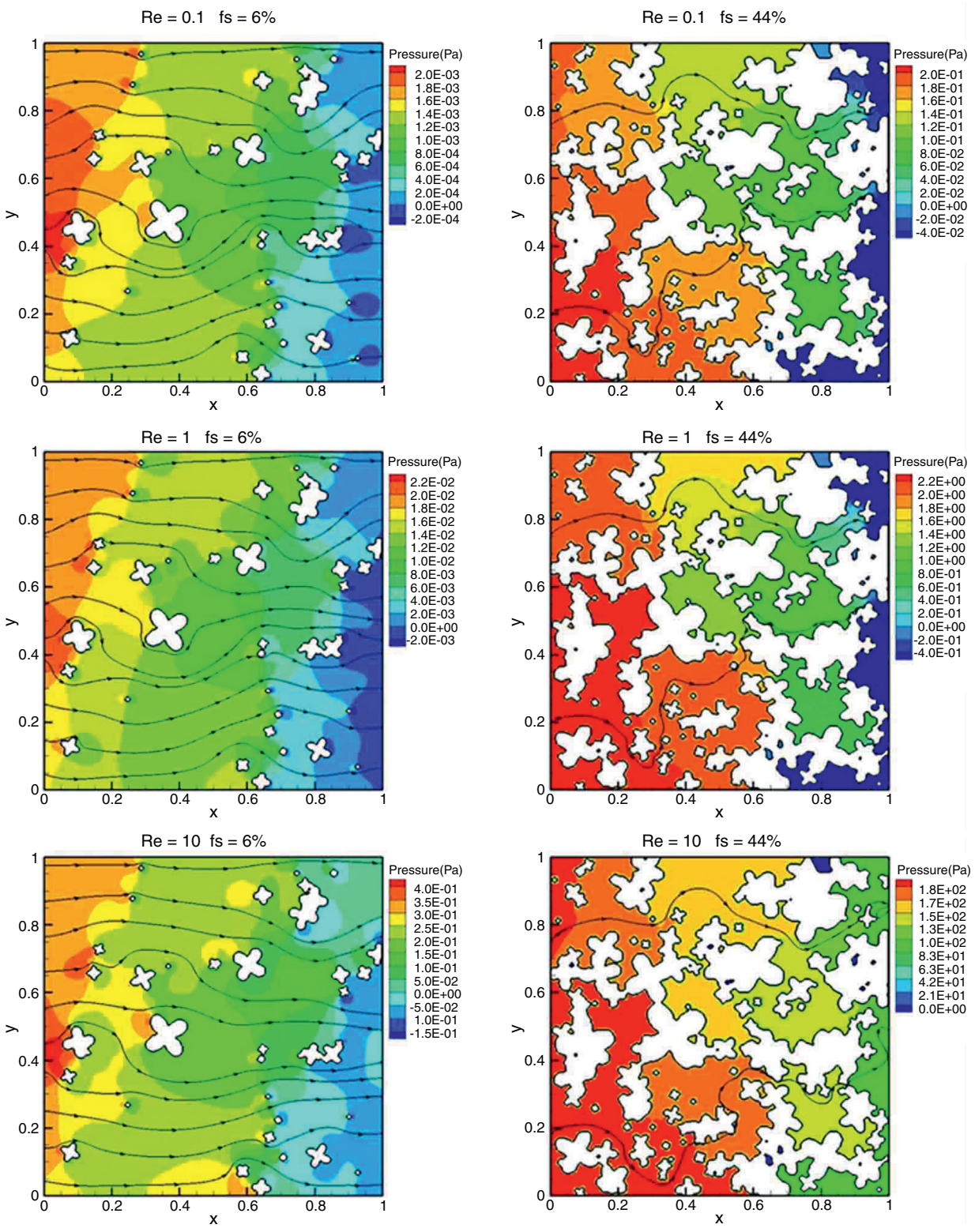

Fig. 9 – Simulation of the pressure field for three *Re* numbers, 0.1, 1, and 10 for low solid fraction 0.06 (left) and high solid fraction 0.44 (Right), respectively at cooling rate of 100 J/s in each time step, A356 aluminum alloy, dimensions: x = y = 1 mm.

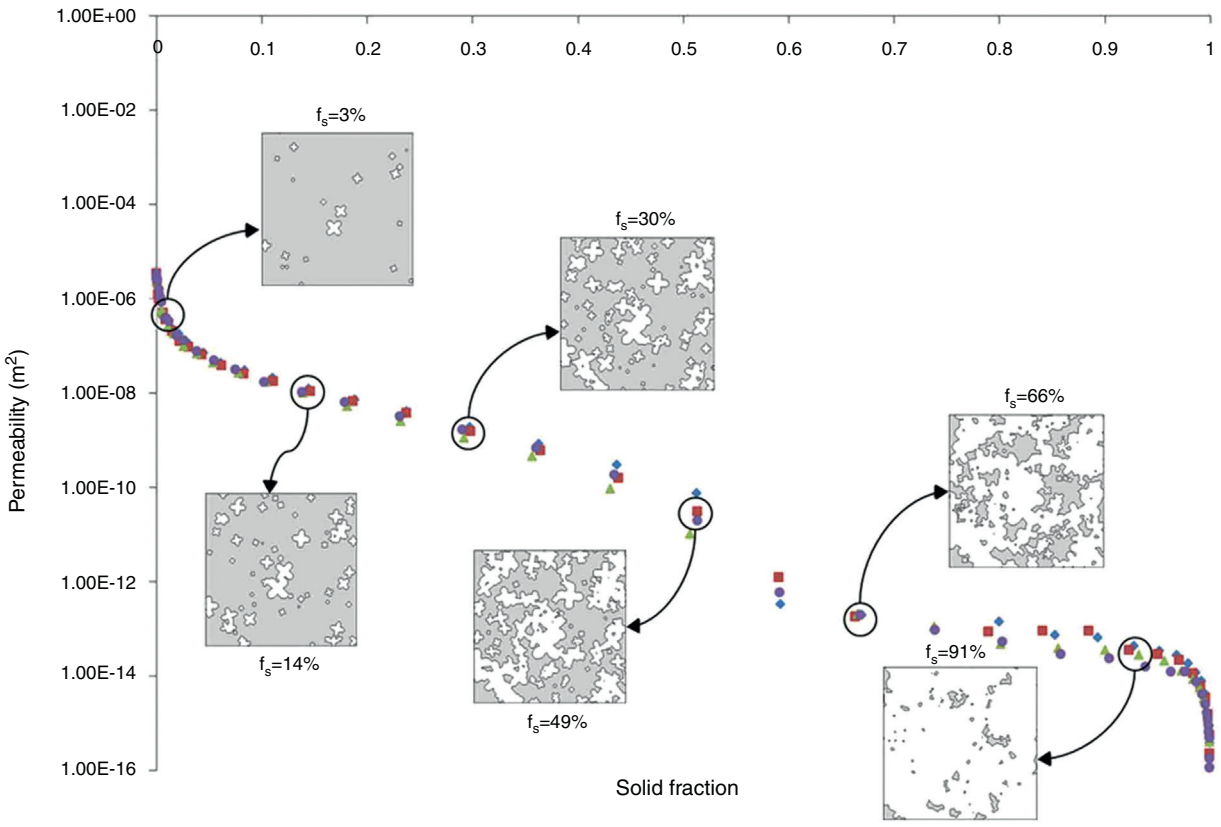

Fig. 10 – Permeability versus solid fraction for A356 aluminum alloy based on simulation results of the present CFD and CA-FV codes during grain growth with 4 random nuclei distribution denoted with ■, ●, ▲, and ◊; *Re* = 0.1 and *dQ* = 100 J/s in each time step.

3.2. *Simulation with ProCast*

Numerical model in parasolid format was imported. Model was meshed by tetrahedral mesh. Preprocess setup with precast. Aluminum A356 was poured in metal mold and cooled with air convection.

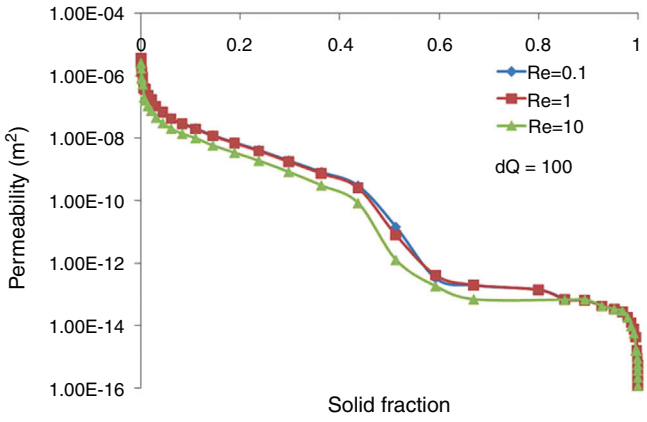

Fig. 11 – Permeability versus solid fraction of the A356 aluminum alloy based on simulation results of the present CFD and CA-FV codes during grain growth for three Reynolds number 0.1, 1, and 10, and cooling of *dQ* = 100 J/s in each time step.

3.3. *Casting*

Aluminum A356 ingot was melted in electrical induction furnace. Mold was milled from cast iron. Melted alloy pored at 700 °C in mold. After solidification, the part was cut from

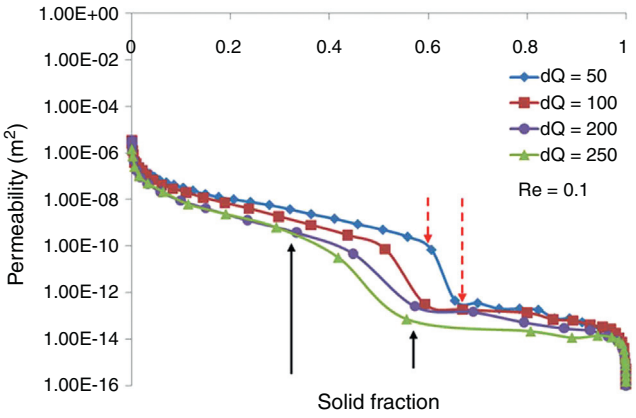

Fig. 12 – Permeability versus solid fraction of the A356 aluminum alloy based on simulation results of the present CFD and CA-FV codes during grain growth with cooling rates between 50 and 250 J/s in each time step at creeping flow range (*Re* = 0.1). Dashed and solid arrows represent a narrow and wide fluctuation range in the permeability for low and high cooling rate, respectively.

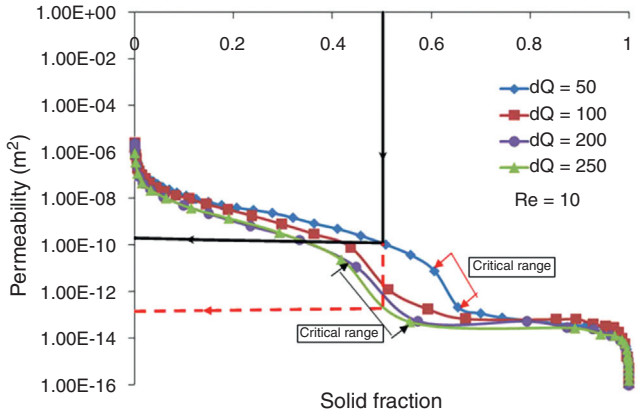

Fig. 13 – Permeability versus solid fraction of the A356 aluminum alloy based on simulation results of the present CFD and CA-FV codes during grain growth with cooling rates between 50 and 250 J/s in each time step at creeping flow range (*Re* = 10).

centerline, polished, etched and a metallography picture was captured from specified a location (Fig. 5).

4. Results

The main parameters that affect the pressure field are the grain distribution, cooling rate and Reynolds number, which are presented below.

1. *Grain distribution*: because of the drag force of the nucleus on fluid flow, distribution and location of the grains affect the pressure field. Fig. 6 shows the effect of grains distribution on the pressure field with two random distributions for three constant solid fractions, 0.1, 0.35, and 0.75 at a fixed cooling rate of 100 J/s in each time step, and *Re* of 0.1.

2. *Cooling rate*: Figs. 7 and 8 show the effect of four cooling rates, 50, 100, 200 and 300 on the pressure field for a low solid fraction ($f_s = 0.2$) and a high fraction solid ($f_s = 0.55$), and *Re* of 0.1.

3. *Reynolds number*: Fig. 9 shows the effect of three *Re* number, 0.1, 1 and 10 on the pressure fields with a cooling rate of 100 J/s in each time step for a low and high solid fraction, 0.06 and 0.44, respectively.

Fig. 10 shows the temporary micro-permeability based on the solid fraction at 4 random grains distributions for *Re* number 0.1 and *dQ* equal to 100 J/s. The results showed that different distributions had no significant effect on the micro-permeability during solidification. Thereafter, the temporary micro-permeability was calculated from the simulation results of pressure and velocity fields in the creeping flow range of Reynolds numbers of 0.1, 1 and 10. Fig. 11 shows the effect of the Reynolds number on the temporary micro-permeability during the solidification of A356 aluminum alloy with the cooling rate of 100 J/s in each time step.

Figs. 12 and 13 show the effect of temporary micro-permeability versus the solid fractions with a cooling rate from 50 to 250 J/s in each time step with Reynolds equal to 0.1 and 10, respectively.

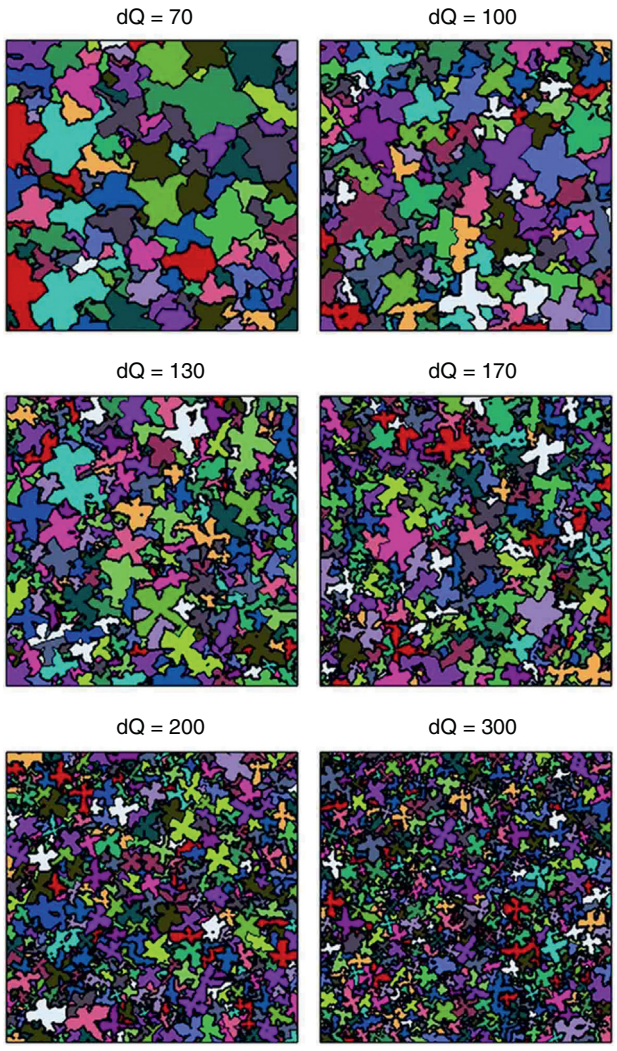

Fig. 14 – Simulation of the grains size, number and distribution after complete solidification of the A356 aluminum alloy for the cooling rates of 70, 100, 130, 170, 200, and 300 J/s in each time step, for a 1 mm × 1 mm domain.

Fig. 14 shows size, numbers, distribution, and morphology of equiaxed grains of A356 aluminum alloy after complete solidification at different cooling rates for a 1 mm × 1 mm domain.

Fig. 15 shows the effect of both cooling rate and solid fraction on the permeability in a 3 dimensional curve for demonstration of the critical range.

Fig. 16 shows the effect of variations of cooling rates on the surface roughness (or dendritic morphology) for an equiaxed grain during grain growth.

Fig. 17 shows the comparison between two Micro and Macro shrinkage porosity models that developed based on the critical permeability in this investigation.

Fig. 18 shows the micro porosity distribution evaluated by developed code.

Fig. 19 shows porosity prediction by ProCast software.

Fig. 20 shows porosity prediction by Niyama criteria calculated in ProCast software.

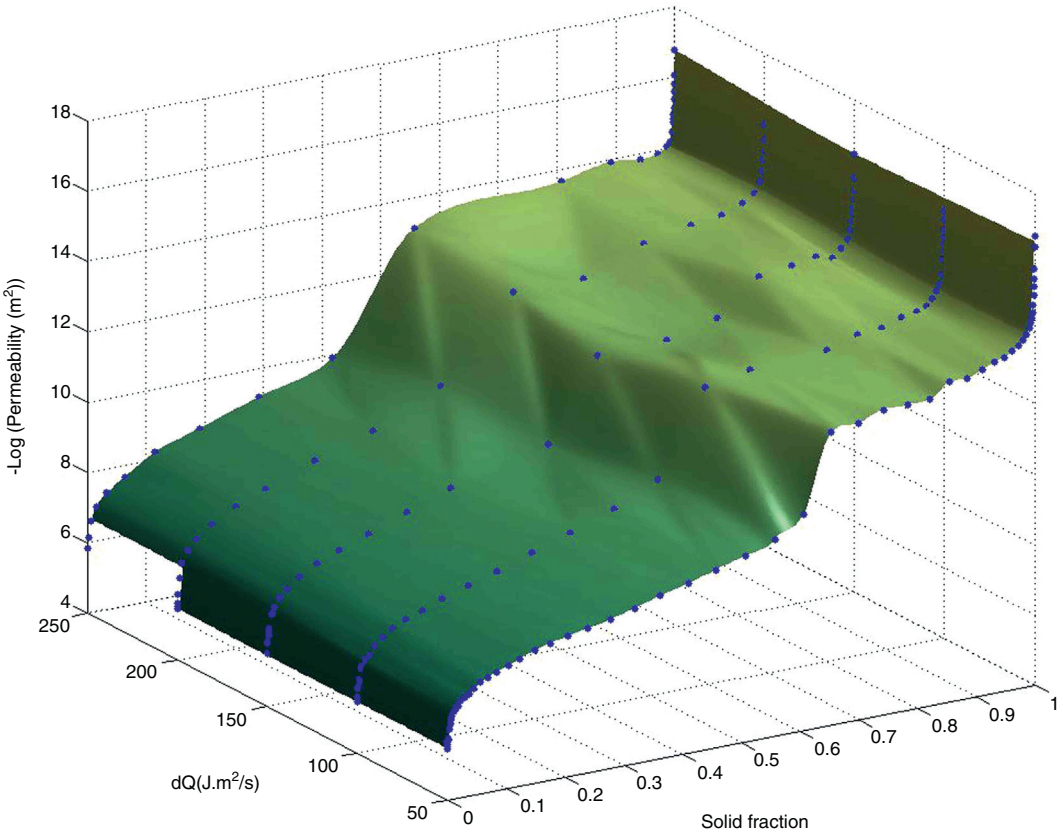

Fig. 15 – Evolution of the solid/liquid interface morphology with increasing cooling rate from left to right.

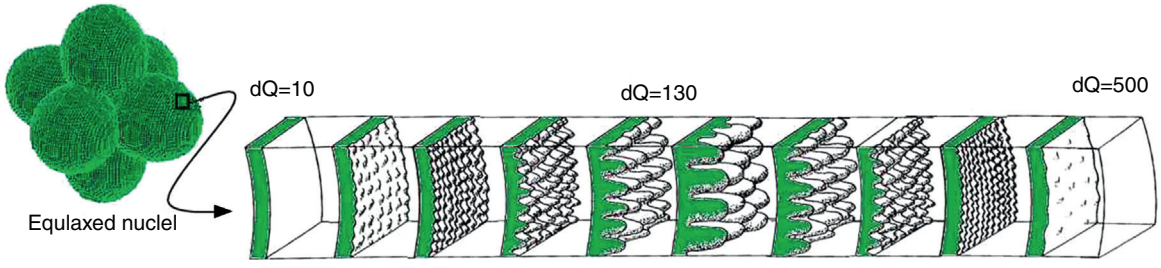

Fig. 16 – Effect of the solid fraction and the cooling rate on the permeability of A356 aluminum alloy.

Fig. 21 shows metallography captured pictures.

5. Discussion

Micro-permeability is a function of the velocity field and pressure gradient of the liquid phase. Moreover, cooling rate, nucleation and growth rate, distribution and morphology of grains, and Reynolds number affects the micro-permeability.

Many numerical fluid flow and heat transfer software and casting commercial codes generate the cooling rate ($\partial T/\partial t$), the temperature gradient ($G = Q/k = \partial T/\partial x$), and solidification rate ($\upsilon = \partial f_s/\partial t$) for each computational cell. Nevertheless, it is important to note that the cooling rate is not an independent variable and needs to be determined by the temperature gradient and the solidification rate. The cooling rate can be written as $\partial T/\partial t = (\partial T/\partial x)(\partial x/\partial t) = G{\cdot}\upsilon$. Therefore, if the inter-dendrite micro-permeability is defined as a function of cooling rate, the micro-structure is related to the thermal history in a macro scale, therefore the formation of micro defects could be predicted. Thus, plotting the micro-permeability versus the cooling rate and the solidification rate can be used as a good criterion for modeling the micro-permeability in micro and meso-scales.

The effect of two random grain distributions was simulated on the pressure and velocity field (Fig. 6). It is evident that the pressure values increased nonlinearly with increasing solid fraction in both distributions (see Fig. 6 legend). Since, the temporary micro-permeability has an inverse relationship with the pressure gradient, then the temporary micro-permeability need to have a nonlinear relationship with the solid fraction. From Fig. 10 it appears that there is a power law relation

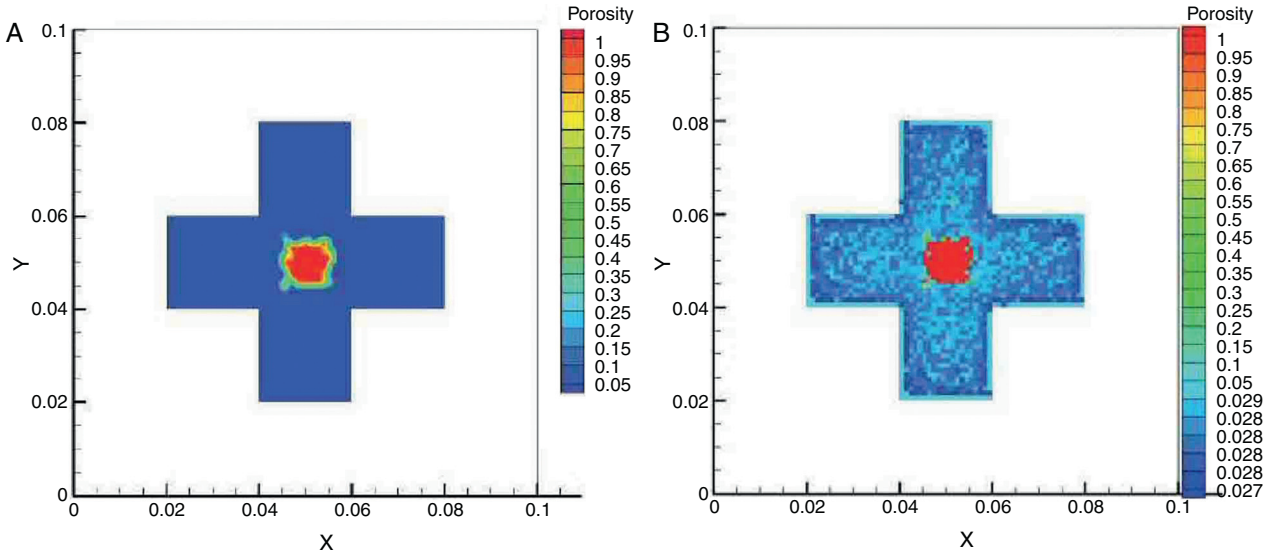

Fig. 17 – Simulation of shrinkage porosities of a casting cross by the present model for A356 aluminum alloy, (a) macro-model, (b) micro and macro model.

between solid fraction and micro-permeability. The markers on Fig. 10 demonstrate that grains distribution did not affect the temporary micro-permeability.

The cooling rate has a significant effect on the pressure field and subsequently on the micro-permeability. It also affects the nucleation and solid fraction rate. This effect was investigated at low and high solid fractions. Results in Figs. 7 and 8 showed that at high solid fraction, pressure fields are more sensitive to the cooling rate in comparison with low solid fraction. Moreover, Figs. 12 and 13 showed the variation in the temporary micro-permeability with the cooling rate at Reynolds number 0.1 and 10, respectively. Figures showed that between 0.33 and 0.66 solid fractions the temporary micro-permeability is very sensitive to the cooling rates. Therefore, these results demonstrate that the cooling rate (dq/dt) and the solidification rate (df_s/dt) control the behavior of the temporary micro-permeability (K) during unconstrained solidification mode.

Finally, the effect of Reynolds number on the pressure fields (Fig. 9) and temporary micro-permeability (Fig. 11) was investigated. These figures showed that increasing the Re numbers in the creeping flow range up to 10 resulted in a decrease in the micro-permeability. Effect of Re number on cooling rate, and solidification rate on the temporary micro-permeability can be observed from comparison between Figs. 11 and 12 for a low and high Re number, respectively. At Re number 0.1, and high cooling rate (250 J/s), critical micro-permeability started at 0.33 solid fractions and finished at 0.60. However, at a lower cooling rate (50 J/s), the critical micro-permeability started at

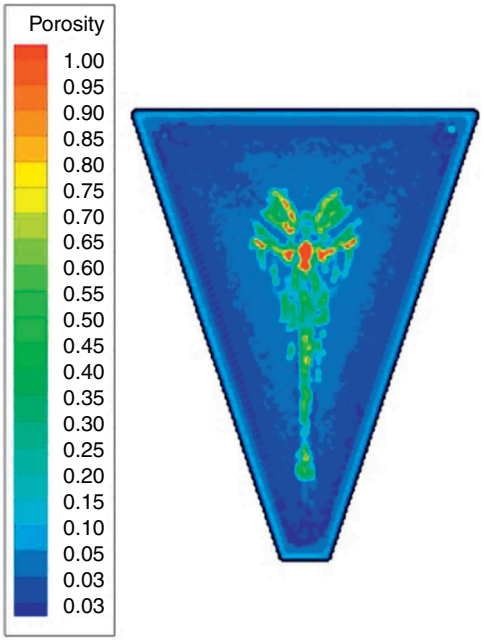

Fig. 18 – Simulation of shrinkage porosities of a casting wedge by developed code for A356 aluminum alloy.

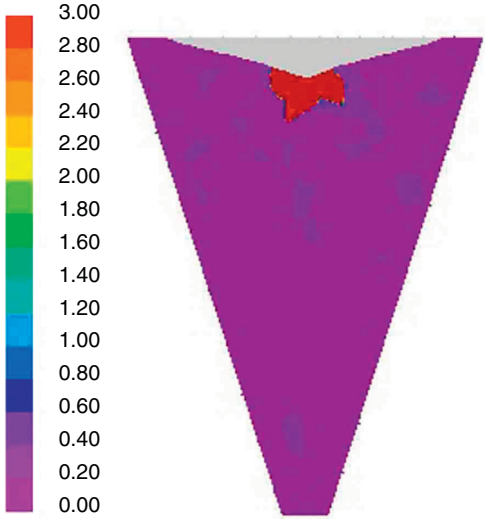

Fig. 19 – Shrinkage porosities of a casting wedge simulated by ProCast software for A356 aluminum alloy.

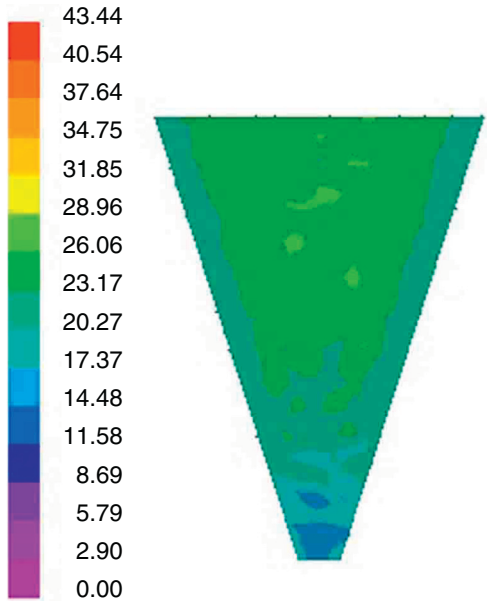

Fig. 20 – Prediction of shrinkage porosities for casting wedge by Niyama criteria calculated in ProCast software for A356 aluminum alloy.

higher solid fraction (0.61) and finished at 0.68. In other words, a narrower range of critical micro-permeability was observed with decreasing the cooling rate, especially at high Reynolds numbers.

Fig. 14 showed the micro structure after complete solidification at different cooling rates. Increasing the cooling rate lead to an increase in the number of nuclei and the change of dendrite morphology from smooth to dendritic surface (surface with high roughness) and that in turn affects the interdendritic micro-permeability. However, beyond a critical cooling rate of about 300 J/s, dendritic surface changes back to a smooth surface (surface with low roughness). This phenomenon has been shown schematically in Fig. 16 that a smooth cloverleaf grain transforms into rough dendrite structure and finally into smooth dendrite cloverleaf.

Finally, the effect of temporary solid fraction (df_s) and heat extraction rate (dQ) on the temporary micro-permeability was modeled as a logarithmic function (Eq. (20)). In this investigation, the temporary micro-permeability results, which was obtained based on the cooling and solidification rate was modeled in a 3-dimensional space. The resulting equation can be used in casting simulation software.

$$-\log(\text{Micro-permeability}) = 8.5f_s + 0.002dQ + 6 \quad (20)$$

In low solid fractions ($f_s < 0.06$) and high solid fractions ($f_s > 0.78$), micro-permeability behaves as an asymptotic function, because of f_l factor in Eq. (14). However between these two solid fractions, behavior of the temporary micro-permeability is complex. In fact this is a new micro-model that can predict micro porosities based on the critical permeability.

As observed in Fig. 12 the critical permeability range (marked with arrows), for formation of the micro-shrinkage, changes by increasing of the cooling rate. It was observed in Fig. 13, that the critical range is wider at high cooling rate than at low cooling rate. For example in Fig. 13, at a fixed solid fraction, 0.5, for two different cooling rates 50 and 250 J/s, the critical permeabilities are approximately 10^{-10} and 10^{-13}, respectively. In other words, for a fixed solid fraction value, the critical permeability is changed by 3 orders of magnitude. This difference is related to the morphology of equiaxed dendrites, which in turn is dependent on the cooling rate and the value of local thermal under-cooling.

Fig. 15 shows the effect of both cooling rate and solid fraction on the permeability behavior for A356 aluminum alloy. The significance of the 3D curve (or Eq. (20)) is that the permeabilities belong to a very fine domain. As a result, it can be used for all meshes of a commercial solidification code, which together forms a macro-model. Therefore during running the commercial codes, when solid fraction for a computational cell becomes greater than zero, the present model, Eq. (20), is called as a subroutine in each time step. The function of this subroutine is to assess the thermal history and cooling rate for this solid fraction. In a given cooling rate and solid fraction, calculated based on the neighboring cells, if the value of permeability lies within the range of critical permeability, then this cell is susceptible to shrinkage porosity. This subroutine is only used for meshes in the solid–liquid interface and their neighboring cells. In fact, there are narrow thermal boundary layers around nuclei that have Newtonian condition and $\partial(\Delta T)/\partial n = 0$; where "$n$" is the normal vector of the liquid–solid interface. This boundary layer can be approximated by thermal characteristic length as, $\delta_T = \alpha/v$, where α is the thermal diffusivity at the nuclei interfaces (see Fig. 1). Thus, in a fixed solid fraction, the cooling rate should be denoted in order to realize the susceptibility of the cell to porosity. If the permeability based on Eq. (20) or Fig. 15, is positioned in the critical range of permeability, then the cell is susceptible to porosity; otherwise the cell will be free of porosity. Finally, a casting cross sample was simulated, once without using the micro shrinkage subroutine, Fig. 17(a), and once using the micro shrinkage model subroutine based on the results in Figs. 15 and 17(b). Fig. 17(b) shows a fine distribution of porosity in all meshes of the system domain, observed as color contours, which is in agreement with real samples and provides a more realistic description of the sample than the current commercial code results.

By casting the wedge part, it is seen that in part centerline micro shrinkage was formed. The porosity density increased from down to up. While in simulation such defects are less predictable. Most commercial software uses for prediction macro shrinkage. As shown in Fig. 19 ProCast shrinkage prediction is less than in Fig. 18 which was predicted in this research. Niyama criteria is really good for micro shrinkage prediction but it is not yet useful for a range of alloys, as shown in Fig. 20. Also, Niyama error in the down part of Fig. 20 is too high. By comparing the simulation results with metallographic cross-section can be stated that the results predicted by this research method are closer to reality. In Figs. 17(b) and 18 meshes with red color contours are the macro porosity defects and the light blue colors contours are the parts susceptible to micro shrinkage porosity. The ultra-fine shrinkage porosities may not be assumed as defects, which depend on application of casting part and its designer opinion. Therefore the present model

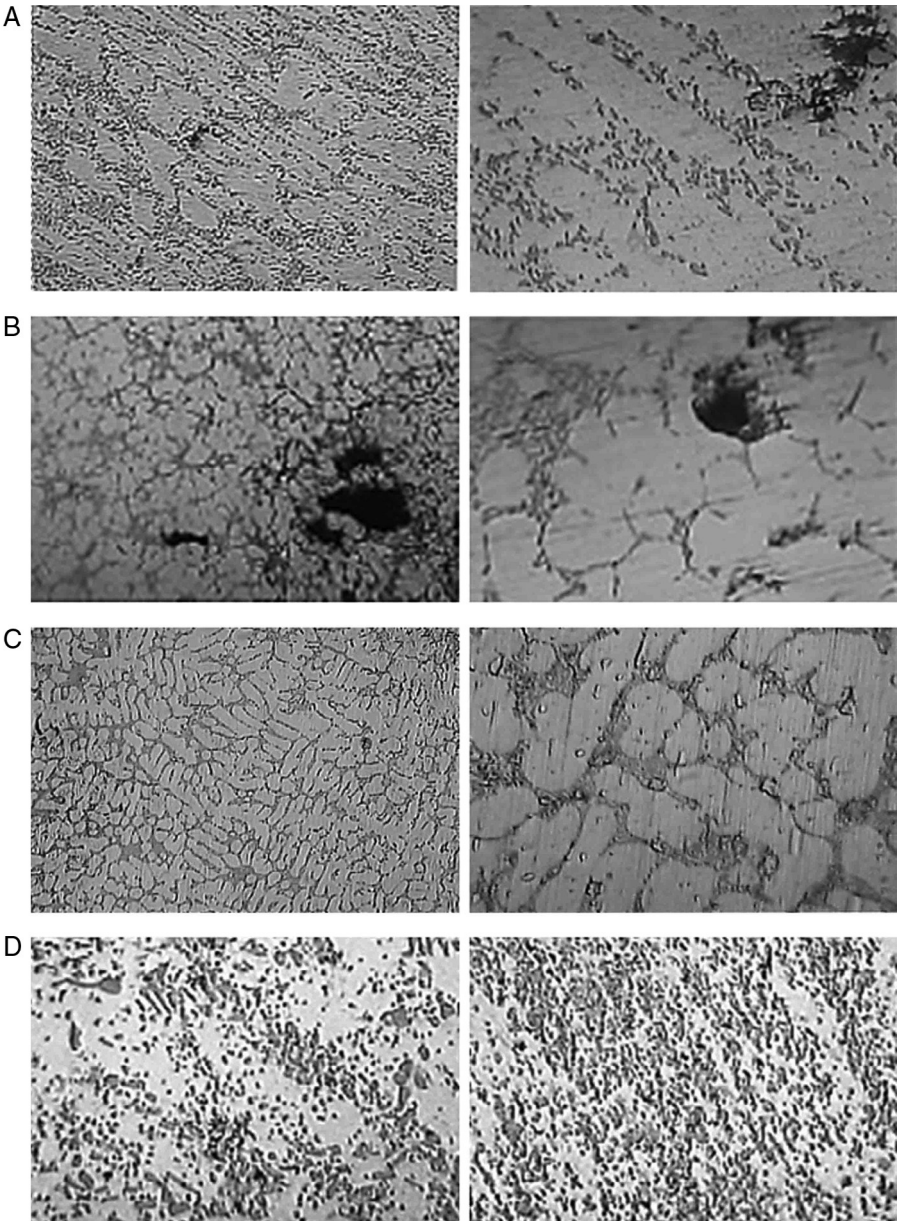

Fig. 21 – Shrinkage porosities for A356 aluminum alloy casting wedge.

for predicting the Micro-Macro porosity defects can be used to commercial solidification and casting codes and improves their accuracy in the field of shrinkage porosity simulation.

6. Conclusions

1. In this investigation, using results obtained from coupling the CFD and CA-FV codes, a relationship was developed between solid fraction and cooling rate versus micro-permeability, in which the constants of this equation is a function of Reynolds number.
2. Simulation results showed that there are fluctuations in micro-permeability in the range of 0.33–0.66, and 0.60–0.66 solid fractions with decreasing cooling rate, in which the shift in the critical range is due to the change in Reynolds number.
3. Beyond a critical cooling rate, ultra fine and smooth equiaxed grains form with low perturbation on their surfaces, which in turn can lead to formation of ultra fine to coarse shrinkage porosities.
4. The constitutive equation of the present code can be utilized in a commercial casting or solidification software for predicting micro and macro shrinkage porosities with improved accuracy.

Conflicts of interest

The authors declare no conflicts of interest.

REFERENCES

[1] Poirier DR. Permeability for flow of interdendritic liquid in columnar-dendritic alloys. Materials Transactions 1987;18B:245–55.
[2] Nandapurkar P, Poirier DR, Heinrich JC. Momentum equation for dendritic solidification. Numerical Heat Transfer 1991;19A:297–311.
[3] Worster MG. Natural convection in a mushy layer. Journal of Fluid Mechanics 1991;224:325–59.
[4] Ganesan S, Poirier DR. Metallurgical and Materials Transactions B 1990;21:173–81.
[5] Carman PC. Fluid flow through a granular bed. Transactions of the Institution of Chemical Engineers 1937;15:150–66.
[6] Williams JG, Morris CEM, Ennis BC. Liquid flow through aligned fiber beds. Polymer Engineering & Science 1974;14:413–9.
[7] Chen YT, Davis HT, Macosko CW. Wetting of fiber mats for composites manufacturing: I. Visualization experiments. AIChE Journal 1995;41:2261–73.
[8] Sangani AS, Acrivos A. Slow flow past periodic arrays of cylinders with application to heat transfer. International Journal of Multiphase Flow 1982;8:193–206.
[9] Sparrow EM, Loefler AL. Longitudinal laminar flow between cylinders arranged in regular array. AIChE Journal 1959;5:325–30.
[10] Larson RE, Higdon JJL. Microscopic flow near the surface of two-dimensional porous media, Part 1. Axial flow. Journal of Fluid Mechanics 1986;166:449–72.
[11] Koch DL, Ladd AJC. Moderate Reynolds number flows through periodic and random arrays of aligned cylinders. Journal of Fluid Mechanics 1997;349:31–66.
[12] Nagelhout D, Bhat MS, Heinricha JC, Poirier DR. Permeability for flow normal to a sparse array of fibres. Materials Science and Engineering A 1995;19:203–8.
[13] Ghaddar CK. On the permeability of unidirectional fibrous media: a parallel computational approach. Physics of Fluids A 1995;7:2563–85.
[14] Eidsath A, Carbonell RG, Whitaker S, Herrmann LR. Dispersion in pulsed systems – III: Comparison between theory and experiments for packed beds. Chemical Engineering Science 1983;38:1803–16.
[15] Thom A, Aplelt CJ. Field computations in engineering and physics. Van Nostrand: London; 1961.
[16] Edwards DA, Shapiro M, Bar-Yoseph P, Shapira M. The influence of Reynolds number upon the apparent permeability of spatially periodic arrays of cylinders. Physics of Fluids A 1990;2:45–60.
[17] Sangani AS, Yao A. Transport processes in random arrays of cylinders. II. Viscous flow. Physics of Fluids 1988;31:2435–42.
[18] Cai Z, Berdichevsky AL. Numerical simulation on the permeability variations of a fiber assembly. Polymer Composites 1993;14:529–39.
[19] McCartney JF. Flow through arrays of cylinders: lattice gas cellular automata simulations. Physics of Fluids 1994;6:435–7.
[20] Sangani AS, Mo G. Inclusion of lubrication forces in dynamic simulations. Physics of Fluids 1994;6:1653–62.
[21] Streat N, Weinberg F. Interdendritic fluid flow in a lead-tin alloy. Metallurgical and Materials Transactions B 1976;7:417–23.
[22] Murakami K, Shiraishi A, Okamoto T. Interdendritic fluid flow normal to primary dendrite-arms in cubic alloys. Acta Metallurgica 1983;31:1417–24.
[23] Murakami K, Shiraishi A, Okamoto T. Fluid flow in interdendritic space in cubic alloys. Acta Metallurgica 1984;32:1423–8.
[24] Apelian D, Flemings MC, Mehrabian R. Specific permeability of partially solidified dendritic networks of Al-Si alloys. Metallurgical and Materials Transactions B 1974;5:2533–7.
[25] Poirier DR, Ocansey P. Permeability for flow of liquid through equiaxial mushy zones. Materials Science and Engineering A 1993;171:231–40.
[26] Duncan AJ, Han Q, Viswanathan S. Measurement of liquid permeability in the mushy zones of aluminum-copper alloys. Metallurgical and Materials Transactions B 1999;30:745–50.
[27] Nielsen O, Mo A, Applolaire B, Combeau H. Measurements and modeling of the microstructural morphology during equiaxed solidification of Al-Cu alloys. Metallurgical and Materials Transactions A 2001;32:12049–60.
[28] Piwonka TS, Flemings MC. Part VIII – Pore formation in solidification. Transactions of the Metallurgical Society of AIME 1966;236:1157–65.
[29] Liu CY, Murakami K, Okamoto T. Permeability of dendrite network of cubic alloys. Materials Science and Technology 1989;5:1148–52.
[30] Brown SGR, Spittle JA, Walden-Bevan R. Numerical determination of liquid flow permeabilities for equiaxed dendritic structures. Acta Materialia 2002;50:1559–69.
[31] Madison J, Spowart J, Rowenhorst D, Aagesen LK, Thornton K, Pollock TM. Modeling fluid flow in tree-dimensional single crystal dendritic structure. Acta Materialia 2010;58:2864–75.
[32] Atwood RC, Lee PD. A combined cellular automaton and diffusion model for the prediction of porosity formation during solidification. In: Sahm PR, Hansen PN, Conley JG, editors. Modelling of casting welding and advanced solidification processing IX. Aachen: GER; 2000. p. 2–9.
[33] Lee PD, Chirazi A, See D. Modeling microporosity in aluminum-silicon alloys: a review. Journal of Light Metals 2001;1:15–30.
[34] Kurz W, Bezencon C, Gäumann M. Columnar to equiaxed transition in solidification processing. Science Technology and Advance Materials 2001;2:185–91.
[35] Kurz W, Giovanola B, Trivedi R. Theory of microstructural development during rapid solidification. Acta Metallurgica 1986;34:823.
[36] Mirbagheri SMH, Silk J. Simulation of Si concentration effect on the permeability for columnar dendrite structures during solidification of Al-Si alloy. Materials & Design 2007;28:356–61.
[37] An SU, Larionov V, Monastyrski V, Monastyrskaia E, Grafas I, Oh JM, et al. The thermal analysis of the mushy zone and grain structure changes during directional solidification of superalloys. In: Green KA, Pollock TM, Kissinge RD, editors. Superalloys 2000. TMS; 2000. p. 247–54.
[38] Lee PD, Atwood RC, Dashwood RJ, Nagaumi H. Modeling of porosity formation in direct chill cast aluminium-magnesium alloys. Materials Science and Engineering A 2001;21:213–22.
[39] Bahat MS, Poirier DR, Heinrich JC. Permeability for cross flow through columnar-dendritic alloys. Metallurgical and Materials Transactions B 1995;26:1049–56.
[40] Darcy H. Les Fontaines Publiques De Ville de Dijon. Paris: Dalmont; 1856.
[41] Mirbagheri SMH, Ashuri H, Varahram N, Davami P. Simulation of mold filling in lost foam casting process. International Journal of Cast Metals Research 2003;16:554–65.
[42] Griebel M, Dornseifer T, Neunhoeffer T. Numerical simulation in fluid dynamics: a practical introduction. Society for Industrial and Applied Mathematics 1997:1997.
[43] Mirbagheri SMH, Baiani H, Barzegari M, Firoozi S. Simulation of liquid flow permeability for dendritic structures during solidification process. In: Minin IV, Minin OV, editors. Computational fluid dynamics technologies and applications. Rijeka: InTech, CRC; 2011. p. 333–58.